Planetary and Space Science 210 (2022) 105389

Contents lists available at ScienceDirect

Planetary and Space Science

journal homepage: www.elsevier.com/locate/pss

Morphological analyses of small and medium size landforms in Scandia Cavi and Olympia Undae, Northern circumpolar region of mars

Marina Sánchez-Bayton [a,*], Miguel Herraiz [a,b], Patrick Martin [c], Beatriz Sánchez-Cano [d], Erwan Tréguier [e], Akos Kereszturi [f,g]

[a] Department of Physics of the Earth and Astrophysics, Universidad Complutense de Madrid (UCM), Madrid, Spain
[b] Instituto de Matemática Interdisciplinar (IMI), Madrid, Spain
[c] ESAC (European Space Astronomy Centre), Villanueva de La Cañada, Spain
[d] School of Physics and Astronomy, University of Leicester, Leicester, UK
[e] Formerly at ESAC (European Space Astronomy Centre), Villanueva de La Cañada, Spain
[f] Research Centre for Astronomy and Earth Sciences, Konkoly Thege Miklos Astronomical Institute, Hungary
[g] European Astrobiology Institute, Hungary

ARTICLE INFO

Keywords:
Mars
Volcanic landforms
Scandia cavi
Olympia undae

ABSTRACT

This article presents a systematic morphological analysis of the topographic landforms at Olympia Undae and Scandia Cavi in the northern circumpolar region of Mars. The study has been performed using images from Mars Express and Mars Reconnaissance Orbiter, as well as topographic profiles from Mars Global Surveyor of 200 small and medium-size geological landforms (16 km diameter on average). The main morphometric parameters of these landforms have allowed their classification into three groups that include cratered structures, non-cratered structures, and complex irregular structures. In the cratered group, three subgroups can be distinguished: cratered cones, impact craters and undifferentiated craters. In turn, the non-cratered group includes two subgroups: peaked domes and simple domes. Their possible relation to internal, surface and impact processes is discussed.

1. Introduction

In this article we conduct a systematic analysis of the morphology and occurrence of topographic landforms in the region of the northern circumpolar area of Mars that spans between 72°-80° N and 150°-230° E. This region includes a small part of Olympia Undae (68.500 km^2) and a large area of Scandia Cavi (302.810 km^2). These two different sized areas show different areal density of landforms that populate them: Olympia Undae has a very low number of visible structures and almost all of them are located close to Scandia Cavi, while the number and variety of landforms is larger in Scandia Cavi and they are scattered throughout the whole area.

Olympia Undae is located in the southern part of Olympia Planum, on its border with Scandia Cavi, and overlaps the deposit of water ice and sand that lie beneath the current ice cap. This zone, known as Cavi unit, is made up of aeolian sand and water ice underlying the Late Amazonian north polar layered deposits. Its strata of Middle to Late Amazonian age constitute a record of wind patterns and past climate (Nerozzi and Holt, 2019). In turn, Cavi unit lies over the Vastitas Borealis Interior Unit (VBIU). The thickness of Cavi unit diminishes towards the south of Olympia Planum. Below Olympia Undae is only several tens of meters thick and disappears below Scandia Cavi that lies over Vastitas Borealis directly. Olympia Undae' surface is composed of migrating dunes and sand sheets with thicknesses ranging between meters and tens of meters while Scandia Cavi is characterized by a very uneven surface. Chronologically, Olympia Undae is composed mainly by Middle to Late Amazonian materials, and Scandia Cavi by Early Amazonian components (Tanaka et al., 2008; Rodriguez et al., 2021).

A map showing the main features of the geology and topography of the study area is displayed in Fig. 1a, where the different structures that are studied in this work are highlighted in pink color. This Figure also contains two elevation and slope profiles that cross both regions and show their different topographic characteristics (Fig. 1b and c). In particular, Olympia Undae is the largest continuous dune field on Mars and covers an area of 470.000 km^2 with an average elevation of 4.250 m below the reference ellipsoid. It presents few well-defined positive topographic features. By contrast, Scandia Cavi, which is located at the southern border of Olympia Undae, is composed of two rugged

* Corresponding author.
E-mail address: marinasanchezbayton@ucm.es (M. Sánchez-Bayton).

https://doi.org/10.1016/j.pss.2021.105389
Received 14 May 2021; Received in revised form 20 November 2021; Accepted 22 November 2021
Available online 27 November 2021

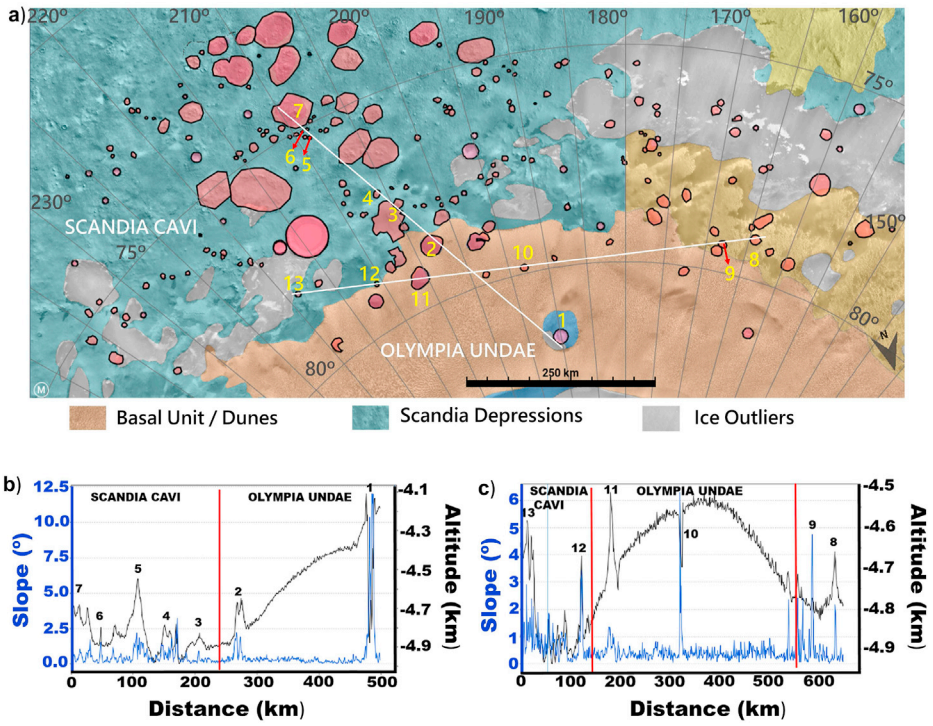

Fig. 1. (a) MOLA-based map of the study area with the 200 landforms studied in this work, superimposed over a 1:15,000,000 geological map from Skinner et al. (2006).(b, c) Topographic (black) and blended slope (blue) profiles with distance crossing different landforms in Olympia Undae and in Scandia Cavi. These two profiles correspond to the lines marked in (a) and offer a quick view of the geologic structures of this study. The border between Scandia Cavi and Olympia Undae is marked with a red vertical line.

mountainous terrains that extend for 200 and 300 km, respectively. It includes irregularly shaped depressions (also called "cavi") surrounded by tens-to hundreds-of-meters-high rough terrain (Tanaka et al., 2003, 2008). Both regions have received increasing attention in recent years because: (1) Olympia Undae is the location of the largest gypsum deposit on Mars to date (Langevin et al., 2005; Fishbaugh et al., 2007; Horgan et al., 2009; Massé et al., 2012) and (2) the presence of mega ripples and seasonal dune movement within Scandia Cavi (Tanaka et al., 2003, 2005, 2008; Boazman et al., 2020). Since the formation of gypsum (hydrated Ca sulfate, $CaSO4 \cdot 2H2O$) requires liquid water, its presence sets out new questions about the aqueous history and the geological evolution of the entire region. Theories to explain the origin of the gypsum in the northern polar region include interaction of Ca-rich minerals with water-containing sulfuric acid of volcanic origin (Langevin et al., 2005; Fishbaugh et al., 2007), ice cap melting during warm periods (Langevin et al., 2005), and evaporation of saline waters (Szynkiewicz et al., 2010). A more exhaustive study of the topographic landforms can contribute to significantly improve our understanding of the area, as well as of the role played by volcanism in the origin and evolution of gypsum. Moreover, it may help to identify possible past heat sources that are so far unknown.

Various positive topographic structures such as cones and domes, whose origin may be volcanic, have been previously analyzed in the northern circumpolar region (Garvin et al., 2000a,b; Kneissl and Neukum, 2008; Tanaka et al., 2009; Fagan et al., 2010; Putzig et al., 2018; Krasilnikov et al., 2018). Many of them are particularly difficult to characterize from orbiter images because they have a relatively small size (~2 km), occasionally are affected by sediment covers (such as ice or dunes), or underwent significant erosion. Moreover, the coverage limitation of remote-sensing missions at high latitudes has resulted in fewer high-quality images of the area. Besides, several of these landforms are found very close to or even overlapping each other, making the analysis more complex. However, the main difficulty in the data acquisition comes from the limitations of the available terrain digital elevation models. In this work, we have only used the Mars Orbiter Laser Altimeter (MOLA) data supported by High Resolution Stereo Camera (HRSC) and Context Camera (CTX) images. These datasets will be explained in more detail in the next Section.

In this study, we select 200 small and medium-size landforms (their diameter varies between 3 and 68 km, being on average 16 km) from the Olympia Undae and Scandia Cavi areas. All landforms are located between 4300 and 4900 m elevation below the MOLA Martian reference datum (Smith and Zuber, 1999). The main objective is to identify, characterize and catalogue these landforms, which are of special interest for understanding the overall history and evolution of the area, one of the youngest parts of the planet (Weiss, 2019). To that end, 1477 images from Mars Express (MEX) and Mars Reconnaissance Orbiter (MRO) are analyzed, together with topographic information. We categorized each of the structures in three groups based on the presence (or lack) of a visible crater in the images, and on their topographic characteristics. As described later in the paper, these groups are: cratered-structures, non-cratered structures and irregular structures. Then, we perform a comprehensive analysis of their topographic characteristics to evaluate three possible origins: (1) "internal" such as subsurface processes, e.g. volcanic activity, (2) "surface processes", when the phenomena occur either above the surface or close to it, such as aeolian processes driving erosion or deposition, or near the subsurface such as sublimation and subglacial processes, and (3) "impact"-related, when the process is originated from an impact event.

2. Datasets

This research uses orbital images of the northern polar region from different cameras, such as the High Resolution Stereo Camera (HRSC) (Neukum et al., 2004a,b) onboard MEX (Chicarro et al., 2004) and the Context Camera (CTX) (Malin et al., 2007) onboard MRO. The HRSC camera has a basic resolution of 10–20 m/pixel in stereo that can be increased to 2–5 m/pixel when Super-Resolution Channel (SRC) is activated. HRSC images cover nearly the entire Martian surface. This instrument allows analyzing details down to 10–30 m. In this study, we use 221 different radiometrically calibrated HRSC Nadir images of Level 3 (photometrically normalized). CTX are black-and-white images with a spatial resolution of 6 m/pixel (Malin et al., 2007) with a good coverage of the planet entire surface. We have used 1205 images of this kind. We have also used 51 images obtained by the High Resolution Imaging

Science Experiment (HiRISE) (McEwen et al., 2010) on board MRO that partially cover 18 of our landforms.

The topographic information comes from the digital elevation model (DEM) and digital terrain model (DTM) based on data from the Mars Orbiter Laser Altimeter (MOLA; Smith et al., 2001) onboard Mars Global Surveyor (MGS). This instrument achieves precise topographic information of the Martian surface by measuring the time of flight of laser pulses sent by the instrument to the surface and then back to the spacecraft at a rate of 10 Hz. MOLA provides measurements of the topography of Mars with a surface spot size of approximately 120 m. The center-to-center along-track footprint is 330 m and the vertical accuracy, including the radial orbital error, is 10 m (Smith et al., 2001). The topography is expressed in IAU2000 planetocentric coordinates referenced to the latest Mars gravity model (Smith et al., 1999).

3. Methodology

We focus on small and medium-size landforms with diameters between 3 and 68 km that are covered by enough images and topographic profiles of good quality. Thus, a set of 200 landforms was selected. Concerning the size, 86 (43%) of the chosen structures have a basal area smaller than 50 km^2, and 27 (24%) of the 114 remaining structures are smaller than 100 km^2. With respect to the location, 23 topographic landforms are situated in Olympia Undae and 177 in Scandia Cavi. The lesser number of landforms found in Olympia Undae can be due to the sand coverage there, and to the different geological history (Krasilnikov et al., 2018). Fig. 1a shows the distribution of these 200 landforms, whose main morphological parameters are displayed in Fig. 2a–d and will be explained below.

The data analysis is performed using the JMARS (Java Mission-planning and Analysis for Remote Sensing) software tool (Christensen et al., 2009). This is a geospatial information system (GIS) based software that provides data-analysis tools for NASA Mars missions such as MGS, from which the MOLA data are obtained. The JMARS map created for this study is freely available at Sánchez-Bayton et al. (2021) and a full list of acronyms used in this work is available in Table 1. Fig. 2e–j summarize the main steps of the methodology adopted to characterize the structures. The subsequent steps are the following:

- Using the DEM/DTM data in JMARS, the terrain is surveyed in order to find the landforms that have enough observations (both images and topographic data). Landforms with and without craters are separated.
- Using JMARS, a grid of profiles over each structure is made, from which the MOLA topographic altitude is retrieved. The slopes are also obtained from longitude-latitude maps in JMARS (Fig. 2f) retrieved as a blend of the DEM/DTM data derived from MOLA and HRSC data.
- Based on the MOLA retrievals, 2D and 3D views of each landform are created using a gridding and surface mapping software. The joint visual analysis of the 2D/3D orbital view (Fig. 2e) and the 2D topographic map with the terrain elevation in colors (Fig. 2f) give the first approach of the main geomorphological characteristics of the landforms (being cratered or non-cratered structure, degree of complexity, and presence or lack of ejecta). In particular, several morphological parameters such as those highlighted in Fig. 2a–d are retrieved: shortest and longest crater diameter (Scr and Wcr, respectively), Crater Depth (Dcr), shortest and longest basal diameter (Sco and Wco, respectively) and altitude (Hco) with respect to the terrain (base of the structure). This classification follows the same criteria than Brož and Hauber (2013), and Lenhardt et al. (2018) for the nomenclature.
- In order to analyze the nature of each landform, further parameters are also considered. These are maximum (MxE) and minimum (MiE) elevation of the structure and basal area (A). For the analysis of the cratered landforms (Fig. 2a and b) the crater area (Acr) is added and Hco is taken as the highest height from the terrain to the near upper rim measured (Fig. 2a and b). For non-cratered landforms, Hco is measured as the difference MxE-MiE (Fig. 2c and d). The whole set of retrieved parameters is provided in the Supporting Information File.
- Using the derived morphological parameters, the structures are classified according to three groups:

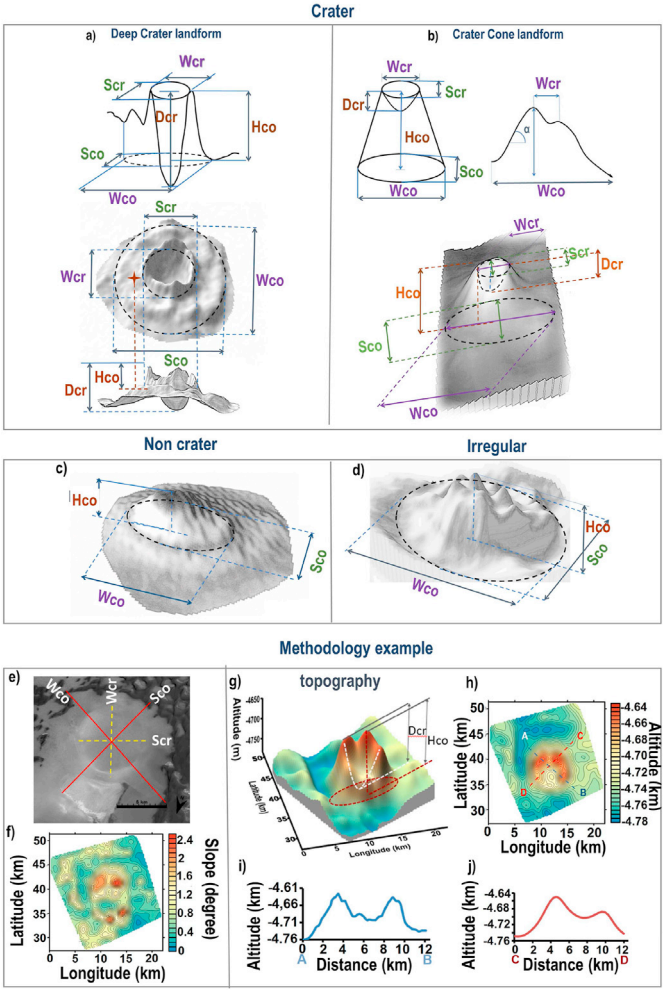

Fig. 2. Top and medium panels: Representation of the different morphological parameters used in this study for the different types of landforms. (a) Structures with a deep crater (Dcr) that is greater than the landform height over the terrain (Hco). Wcr and Scr respectively are the largest and smallest lengths of the crater, and Wco and Sco the largest and smallest lengths of the base of the structure. (b) Same parameters for structures with craters that are less deep than the landform height. (c) Same parameters for structures without crater. (d) Same parameters for irregular structures. Bottom panels: Methodology applied in this study for the same structure: (e) Orbital image of a landform where the morphological parameters described in the first part are marked. (f) 3D topographic map with the terrain elevation in colors. (g) 2D map of blended slopes. (h) 2D topographic map with the terrain elevation in colors. (i, j) Altitude-distance profiles corresponding to the dashed line profiles of panel h. In these profiles, and in all that appear in the following figures, the origin of the X-axis corresponds to the first letter in alphabetical order marked in the corresponding profile line.

- Cratered structures (Fig. 3): For those structures with craters, first, we take into account the depth of the craters and whether they are deeper than the surrounding terrain. Second, we search for the presence of ejecta around the craters. In this group, we can distinguish three subgroups. (1) Cratered Cones (CC): they have a shallow crater above the terrain and no ejecta. (2) Impact craters (IC): they have a deep crater often below the terrain and there is a clear signature of ejecta. (3) Undifferentiated

Table 1
Acronyms used in the article.

CC	Cratered Cones	Dcr	Crater Depth	A	Basal Area	MOLA	Mars Orbiter Laser
IC	Impact Craters	Acr	Crater Area	Hco	Altitude	MEX	Mars Express
UC	Undifferentiated Craters	Wcr	Crater Longest Diameter	Wco	Basal Longest Diameter	HRSC	High Resolution Stereo Camera
PD	Peak Domes	Scr	Crater Shortest Diameter	Sco	Basal Shortest Diameter	MGS	Mars Global Surveyor
SD	Simple Domes	MxE	Maximum Elevation	MiE	Minimum Elevation	CTX	Context Camera
IS	Irregular Structures					MOC	Mars Orbiter Camera
						MRO	Mars Reconnaissance Orbiter

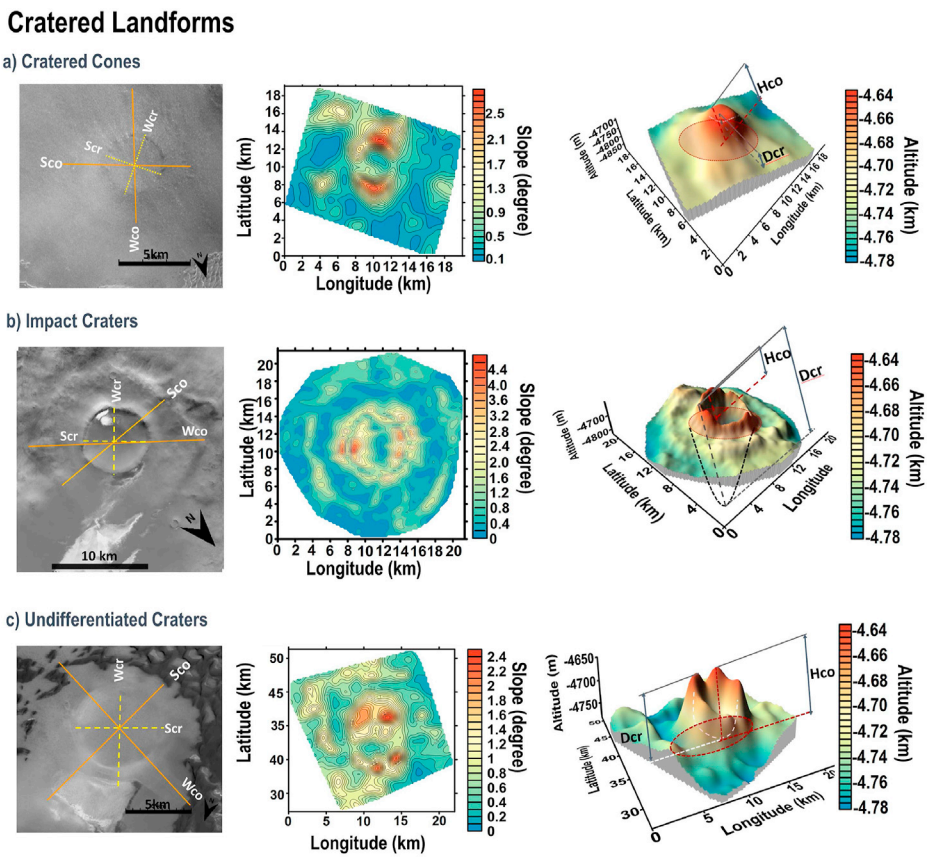

Fig. 3. Representative examples of cratered landforms. a) Cratered cones, b) Impact craters, c) Undifferentiated craters. For all of them, the first column contains an orbital image of the landform with the main morphological parameters defined (same style as in Fig. 2e). The second column shows a 2D map of the structure blended slopes, and the third column a 3D altitude-colored topographic map where several morphological parameters are also marked.

craters (UC): They have mixed characteristics of CCs and ICs.

○ Non-Cratered structures (Fig. 4a–b): Depending on their location, those structures without craters are classified into two subgroups. (1) Peaked Domes (PD): They are situated over Scandia Cavi, have a general peaked shape, and their bases are narrow in comparison to their height. (2) Simple Domes (SD): They are located over Olympia Undae. They have low-medium heights with a dome-shaped upper part without noticeable features in the top and are surrounded by a semi-arc-shaped feature that is lower than the surrounding terrain.

○ Irregular Structures (IS) (Fig. 4c): These structures are situated both over Olympia Undae and Scandia Cavi and are composed by a group of sub-structures considered as elements of a bigger landform instead of individual structures because a larger topographic unit containing the substructures is clearly identified.

A more detailed description of the characteristics of each subgroup is given in the next Section.

Our analysis could be affected by two main sources of errors. The first one is the general uncertainty of the original dataset. The MOLA instrument has a range resolution of 37.5 cm, a range precision of 1–10 m for surface slopes of up to 30°, and an absolute accuracy of 1 m with respect to Mars' center of mass (Aharonson et al., 2001). According to Fagan and Sakimoto (2012), the vertical precision of the MOLA dataset for structural slopes of $< 2°$ is approximately 37 cm, and varies up to 10 m for a 30° slope. This uncertainty does not significantly affect our study because most of the 200 structures only reach a slope value smaller than 9°. Considering the positioning, although the MOLA footprints are approximately 120 m in diameter and are spaced ~330 m apart, analyses indicate that random errors in position are less than 100 m (Smith et al., 2001). The second source of error is related to any possible systematic errors due to the pixel pointing accuracy in JMARS. However, we consider that they may not be significant because horizontal errors between two neighboring MOLA data points are less than 10% of the structure diameter. The average MOLA's along-track spacing is ~330 m and most of the analyzed structures are several kilometers large in horizontal dimensions. However, the uncertainty could be larger for the smallest structures.

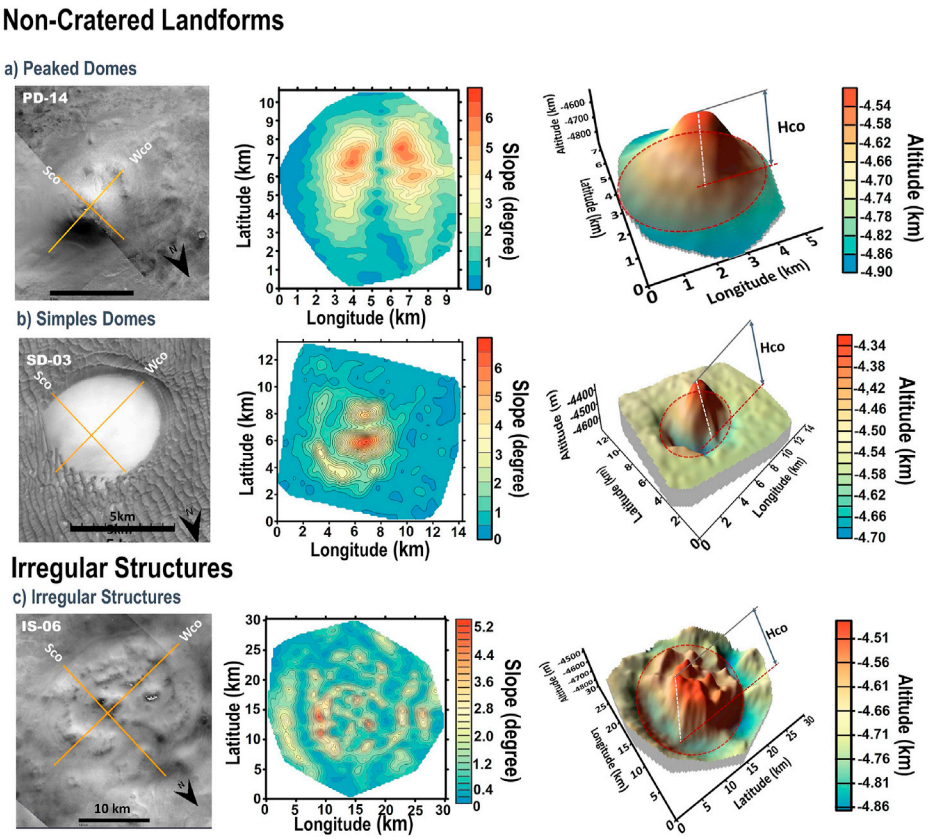

Fig. 4. Representative examples of non-cratered landforms and irregular structures. a) Peaked domes, b) Simple domes, c) Irregular structures. This figure has the same format as Fig. 3.

4. Results

The 200 topographic landforms are catalogued based on their morphology in three groups that include Cratered, Non-Cratered and Irregular Structures. The first two are based on the presence (or lack) of a visual crater in the structure, the third group gathers complex landforms that share some geological and geomorphological properties of the other two. Within the cratered group, three subgroups can be distinguished: Cratered Cones (CC), Impact Craters (IC) and Undifferentiated Craters (UC). In turn, the non-cratered group includes two subgroups: Peaked Domes (PD) and Simple Domes (SD). Figs. 3 and 4 display a representative example of each type and the main parameters obtained in each case. For instance, the first column shows orbital images where the horizontal dimensions on the crater are marked. The second column displays the latitude-longitude map of slopes, and the third column presents the 3D topographic view. Some key morphological parameters have been indicated in these latest plots as complement to the idealized view shown in Fig. 2a–d in order to visualize how each parameter is measured for real structures. The actual parameters are listed in Table 2. Fig. 5a displays the location of the 200 landforms over the study area color-coded by type of subgroup, and Fig. 5b shows their longitude-latitude distribution. Finally, in order to investigate each subgroup characteristics, the ratio Hco/Wco versus area is plotted in Fig. 5c, which separates each subgroup into different clusters with the exception of the UC landforms which do have mixed signatures of other subgroups as described in Section 4.1.3.

Table 2
Summary of main morphometric parameters. A complete list of statistical morphometric parameters is provided in the Supporting Information file.

	CC	IC	UC	PD	SD	IS
Total number	87	30	12	40	6	25
ΔDcr (km)	0.002–0.153	0.013–1.340	0.016–0.204	n/a	n/a	n/a
$\overline{Dcr}$ (km)	0.026	0.194	0.075	n/a	n/a	n/a
ΔHco (km)	0.029–0.568	0.058–0.496	0.042–0.445	0.078–0.679	0.143–0.369	0.218–0.592
$\overline{Hco}$ (km)	0.167	0.162	0,171	0.253	0.220	0.402
$Hco/\ Dcr$	12.87	1.495	3.336	n/a	n/a	n/a
$\overline{Wcr}$ (km)	2.606	8.772	5.258	n/a	n/a	n/a
$\overline{Scr}$ (km)	2.314	8.438	4.850	n/a	n/a	n/a
$\overline{Wco}$ (km)	7.989	21.904	13.742	7.565	8.794	34.176
$Wcr/\ Wco$	0.336	0.474	0.431	n/a	n/a	n/a
$Scr/\ Wcr$	0,88	~1	0.92	n/a	n/a	n/a
$Sco/\ Wco$	0.835	0.959	0.833	0.781	0.768	0.756
ΔAcr (km^2)	0.13–24.97	7.44–354.15	2.670–55.780	n/a	n/a	n/a
$\overline{Acr}$ (km^2)	5.612	76.301	20.009	n/a	n/a	n/a
ΔA (km^2)	4.46–648.40	69.720–2217.780	18.753–1511.070	9.689–318.600	39.300–126.690	152.237–3698.845
$\overline{A}$ (km^2)	75.927	447.834	224.774	43.17	70.090	986.848

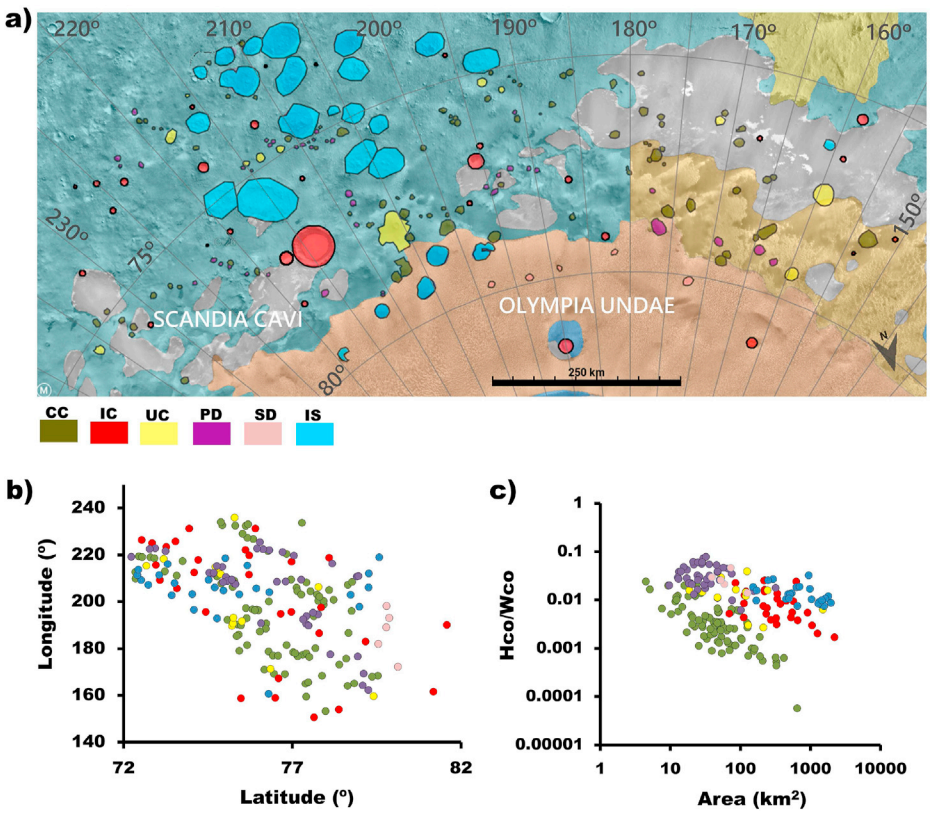

Fig. 5. (a): MOLA-based map showing the 200 landforms represented in Fig. 1a but now highlighted in different colors according to their classification into one of the six different categories: Cratered Cones (CC, in green), Impact Craters (IC, in red), Undifferentiated Craters (UC, in yellow), Peaked Domes (PD, in purple), Simple Domes (SD, in light pink), and Irregular Structures (IS, in blue). (b) Distribution of all landforms of this study in longitude versus latitude. (c) Ratio Hco/Wco versus Area of all the landforms of this study.

4.1. Cratered landforms

This group consists of 129 topographic structures that appear to feature a crater, which are divided in three subgroups: CC, IC and UC. Fig. 6 shows representative examples of images and topographic profiles that are described as follows.

4.1.1. Cratered cones (CC)

This subgroup includes 87 landforms, all of them located in Scandia Cavi (Figs. 1a and 5a). These landforms are elevated with respect to the surrounding terrain and present a well-defined cone shape with one or several small and shallow craters on the summit (but not necessarily at its center). These shallow craters, marked with yellow arrows in Fig. 6, have depths varying between 15 and 100 m. Such small depth can create the visual effect of a flat surface at the top of the cone, but craters are clearly visible in high-resolution images and in topographic profiles. The shapes of the craters are variable, with several irregular and elliptical shapes. Moreover, CCs do not have very steep slopes (Fig. 6) and do not have signs of presence of ejecta. Another characteristic of these landforms is that the crater area, Acr, is smaller than the base, A.

CCs have large variability in size parameters and blended slopes (see Table 2). In particular, crater depth ranges between 0.002 and 0.153 km, being on average 0.026 km (Figs. 3a and 6a), while the average height of the landforms is 0.167 km, which leads to an average Hco/Dcr ratio of 12.87. The craters are not fully circular in general, being their longest dimension, Wcr, on average, 2.606 km, and the shortest, Scr, 2.314 km. The average of the longest dimension of the crater is much smaller than the longest dimension of the base, Wco = 7.989 km. The average ratio

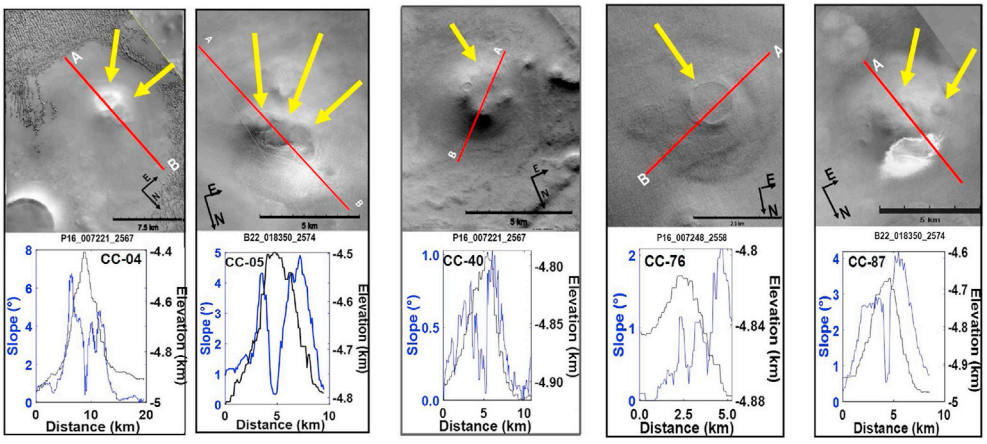

Fig. 6. Representative examples of the Cratered Cones subgroup. Orbital images are shown on the top row and topographic (black) and blended slope (blue) profiles corresponding to the line marked on the images are shown in the bottom row. The yellow arrows in the orbital images point to the crater features.

Wcr/Wco is 0.33. Nevertheless, both the crater and the base are regular in terms of their long and short lengths as the Pearson correlation coefficient R^2 of their linear fits (Wc-Scr and Wco-Sco) is 0.94 and 0.79, respectively. These values underline the homogeneity of this group with respect to their crater and basal shapes. With respect to the area, the craters vary between 0.13 km^2 and 24.97 km^2 with an average of 5.61 km^2 and the bases between 4.46 and 648.40 km^2 giving an average of 75.92 km^2. These results emphasize a characteristic difference between the size of the base and the top of these landforms.

4.1.2. Impact craters (IC)

This subgroup is made of 30 landforms, two are located in Olympia Undae and 28 in Scandia Cavi. We have included a very large crater, named Dokka (IC-05),that has a longest dimension of 52.600 km in comparison to the average Wcr = 8.772 km of the rest of the landforms of this subgroup. Dokka is a well-known crater of meteoritic origin (Conway et al., 2012), with clearly-defined characteristics that we use as a reference to identify other smaller IC structures with similar features and shapes. However, this crater is not included in our statistics as it is a clear outlier in size.

IC landforms are sub-circular depressions that cut into the regional topography with a raised rim. They are relatively easy to distinguish from other subgroups because they have a deep, very circular central crater that is much deeper than the CC ones, and a crater rim above the surrounding terrain. The crater constitutes a large part of the landform, and it is very often surrounded by a notably elevated wall encircled by well-defined ejecta (e.g. Fig. 7). As these features are related to impact processes, we have named them Impact Craters. IC is the only subgroup in this study that has the origin implicit in the name.

Figs. 3b and 7 show examples of this subgroup. For ICs, the crater area varies between 7.44 and 354.15 km^2 with an average of 76.30 km^2 (see Table 2). Most craters are almost perfectly circular, having a ratio of Scr/Wcr~1. They are also notably deep as Dcr ranges from 0.013 to 1.340 km and has an average of 0.194 km. In turn, Hco varies between 0.058 and 0.496 km, and its average is 0.162 km. The ratio Hco/Dcr is 1.49, which is much lower than that of CC (which is 12.87). This low ratio reflects that for 20 out of the 32 ICs, Dcr > Hco and the crater is below the surrounding terrain. Several of these craters can have interior deposits of sand (such as IC-04, Fig. 3b) or ice (such as Dokka, IC-05 in the Supporting Information File).

ICs can look partly similar to CCs because both present a crater feature but they differ in other clear features: IC craters have a perfectly circular shape while CCs typically do not, and, usually, they are accompanied by ejecta, which is not present at all in CCs. In addition, IC craters are deeper and bigger than CCs as can be seen comparing the mean values of Dcr (0.194 km for ICs and 0.026 km for CCs) and Acr (76.30 km^2 for ICs and 5.61 km^2 for CCs).

4.1.3. Undifferentiated craters (UC)

This subgroup is formed by 12 landforms located in Scandia Cavi, all of them with a large and circular central crater that does not cut below the surrounding topography and presents very steep edges.

UCs have mixed morphological characteristics of ICs and CCs (see Table 2). For instance, the large and circular crater (average Scr/Wcr = 0.92) of these structures could be associated with impact processes. The only partial exception is UC-03 that has two craters probably caused by an oblique impact (Fig. 8). In addition, 7 out of the 12 landforms present a clear ejecta (see, for instance, UC-05 in Fig. 8) which is also a distinctive feature of ICs. However, these craters are shallow, with crater depth averaging 0.075 km, and, as CCs, clearly stand above the surrounding terrain. Besides, UC-05 has a topographic profile showing a shape more similar to CCs than to ICs, as can be noted in Fig. 8. Nevertheless, these characteristics do not satisfy the requirements to consider the landforms as either CCs or ICs, in part because the satellite images do not offer enough resolution. Therefore, the classification of these landforms as CCs or ICs is not clear in all cases.

As described below, this characteristic morphological mixture is accompanied by structural parameters that tend to be larger than those of CCs and smaller than those of ICs.

4.1.4. Comparison between CC, IC and UC subgroups

Fig. 9a shows a topographic comparison of three structures of similar size from each of the three subgroups of cratered landforms. It can be noted that UC landforms have intermediate characteristics to those of CC and IC subgroups.

Fig. 9b–d represent the distribution of Hco of all the cratered landforms versus three parameters that describe the crater: depth, area, and largest horizontal dimension. As can be seen, Hco of CCs (green dots) varies between 0.029 and 0.568 km with a mean value of 0.166 km while the variation of ICs (red dots) ranges from 0.058 to 0.496 km and the mean is 0.176 km. Thus, height cannot be a criterion to differentiate them. For UCs, Hco ranges from 0.029 to 0.568 km, and the mean value is also 0.15, i.e. its height variation is intermediate to that of the two other groups. Focusing on the Hco-Dcr pairs (Fig. 9b), there is a clear difference between CCs and ICs, CCs having a smaller Dcr than ICs, and UCs being in between the two groups. UCs landforms show a ratio Hco/Dcr of 3.22 while the values of this ratio for CCs and ICs are 12.87 and 1.49, respectively. This result indicates that the craters of the UC landforms also are above the terrain, but they are not as shallow as the CC landforms. A similar differentiation between CCs and ICs is shown in Fig. 9c, where the Hco versus Acr variation is represented. This Figure clearly indicates that ICs have larger Acr values than CCs, 20 km^2, being on

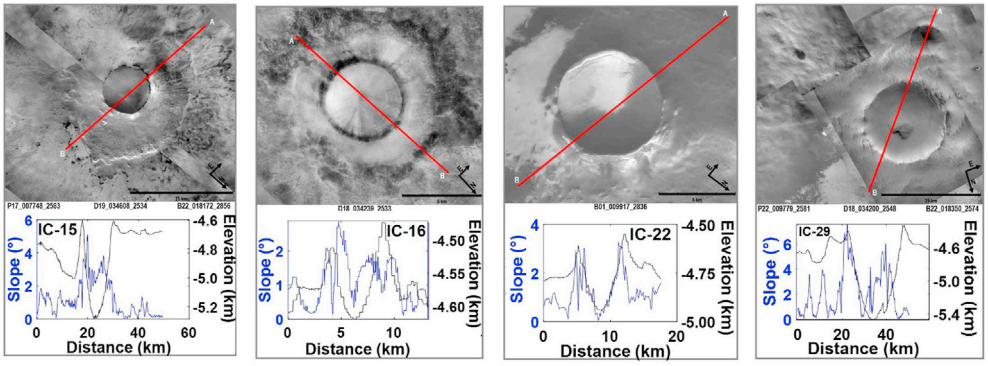

Fig. 7. Representative examples of the Impact Craters subgroup. Orbital images are shown on the top row and topographic (black) and blended slope (blue) profiles corresponding to the line marked on the images are shown in the bottom row. The yellow arrows in the orbital images point to the crater features.

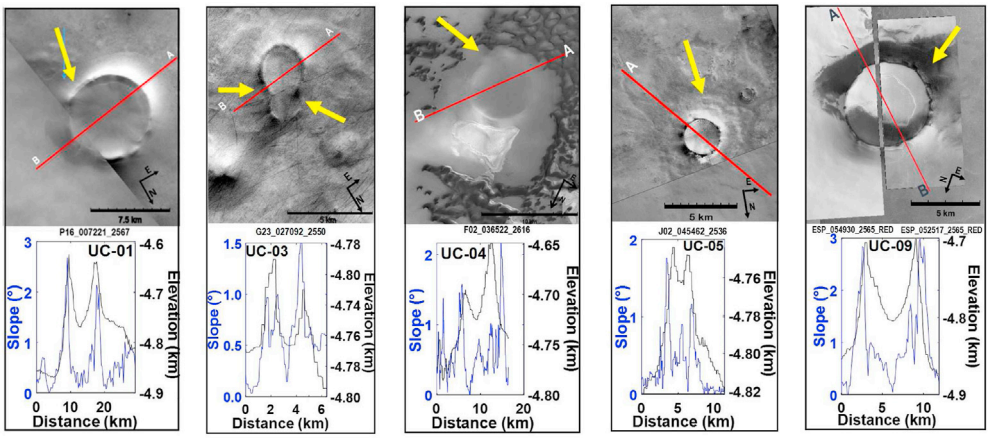

Fig. 8. Representative examples of the Undifferentiated Craters subgroup. Orbital images are shown on the top row and topographic (black) and blended slope (blue) profiles corresponding to the line marked on the images are shown in the bottom row. The yellow arrows in the orbital images point to the crater features.

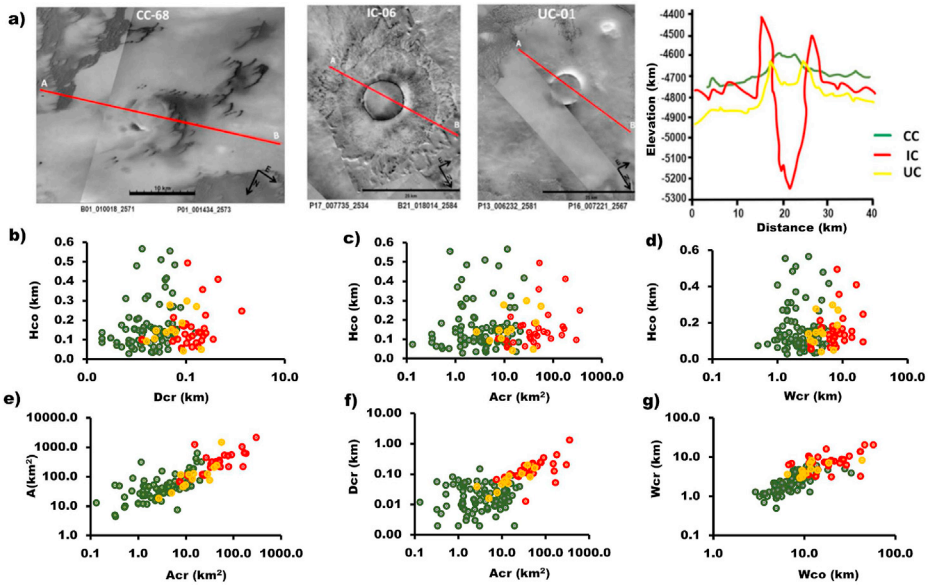

Fig. 9. (a) Comparison of three representative landforms belonging to the different subgroups of cratered landforms: CC-68 (green), IC-06 (red), and UC-01 (yellow). The three orbital images and a comparison of their altitude profiles are shown. (b) Hco versus Dcr for all cratered landforms. (c) Same for Hco versus Acr, (d) Hco versus Wcr, (e) A versus Acr. (f) Dcr versus Acr, and (g) Wcr versus Wco.

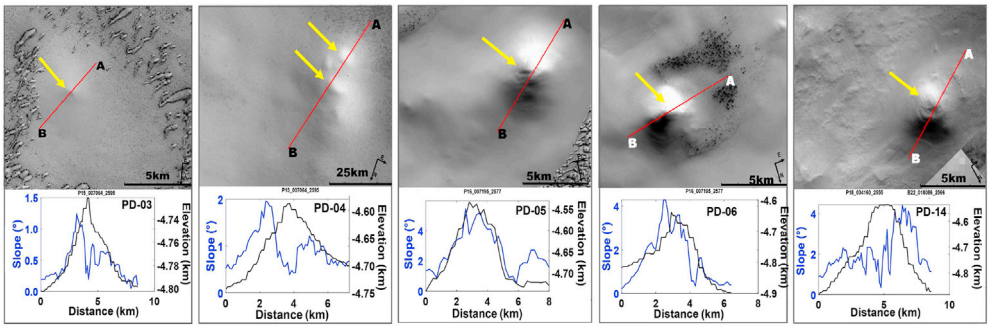

Fig. 10. Representative examples of the Peak Domes subgroup. Orbital images are shown on the top row and topographic (black) and blended slope (blue) profiles corresponding to the line marked on the images are shown in the bottom row. The yellow arrows in the orbital images point to the peaked features.

average, the limit that separates both groups. UC landforms continue occupying positions between these two groups. Something alike happens in Fig. 9d that represents Hco versus Wcr where ICs show larger values of Wcr than CCs (the averages are 8.772 km for ICs and 2.606 km for CCs) and UCs are situated between these two subgroups.

Moreover, in order to show the landform steepness and provide other criterion to better distinguish the three subgroups, Fig. 9e–g show the A-Acr, Dcr-Acr, and Wcr-Wco relations. As can be seen, the three plots display a clear distinction between CCs and ICs and an intermediate position for UCs.

4.2. Non-cratered landforms

The group of landforms without evidence of a crater-like feature within the structure includes 46 topographic positive landforms that we name with the generic term of domes. We note that Cones is another possible term that could be used for some of these structures, but taking into account that their interior is clearly above the terrain and they adopt varied shapes (spherical to ellipsoidal, rounded, elongated) we consider that the term domes reflect their nature better. Figs. 10–12 show representative examples of images and topographic profiles of subgroups that are described below.

4.2.1. Peaked domes (PD)

All the 40 positive topographic landforms that compose this subgroup are located in Scandia Cavi. They are undulated and steep-sided structures with one (e.g., PD-03, PD-05, PD-06, Fig. 10) or several peaks, marked with yellow arrows (e.g., PD-04, Fig. 10), but without craters. Many of these structures resemble a conical shape (Fig. 10) and, in some cases, can be mistaken as CCs. However, they are differentiated from this subgroup of cratered landforms because PDs lack a summit depression (i.e., craters), have steeper walls than CCs, and their basal areas, that yield an average value of 43.17 km^2, are smaller than those of CCs whose average is 75.92 km^2 (see Table 2). The Hco and Wco averages of PD landforms are 0.253 and 7.565 km, respectively, with an average Sco/Wco ratio of 0.78 as they occasionally show a circular shape (e.g., PD-03, PD-05 and PD-14, Fig. 10). PDs can occur as isolated structures situated close to Olympia Undae such as PD-03, or as landmarks placed among other small landforms such as PD-05 and PD-06.

4.2.2. Simple domes (SD)

This subgroup is composed of 6 landforms (Fig. 11) that follow a longitudinal alignment near 80° latitude in Olympia Undae (Fig. 5) and present several characteristic features. They have low-medium heights with a domical-shaped upper part without noticeable features at the top. They also share a characteristic asymmetry with a lower rim toward the southwest, opposite to the higher rim in the northeast at all cross-sectional profiles (see pink shadow area and slope profiles in Fig. 11). SDs have a predominantly circular basal shape, although part of their structure is covered by dunes, and only an arc-shaped zone is visible (Fig. 11). A surrounding trench, which depth can reach an average value of 100 m, can be observed in SD-02, SD-03, SD-04 and SD-05 occupying half of the perimeter of the landform. The SDs subgroup contains the smallest landforms of Olympia Undae of our sample and their area varies between 39.30 km^2 (SD-04 and SD-05) and 126.69 km^2 (SD-01) with an average of 70.09 km^2 (see Table 2). The Hco and Wco averages are 0.220 km and 8.794 km, respectively. This type of structures is not found in Scandia Cavi as they are difficult to identify in such rugged terrain that contains a large number of landforms that can hide these small structures.

4.3. Irregular structures (IS)

This category encompasses the remaining 25 landforms, some of them studied previously by Tanaka et al. (2003) in their analysis of Scandia Tholi and Cavi, and the south of Olympia Planitia, zones that form a region broader than our study area. Five of these 25 landforms are located in Olympia Undae (IS 01–05) and the rest in Scandia Cavi (IS 06–25).

These landforms are the biggest structures analyzed in this study, and are named Irregular Structures (IS) here, because of their very irregular shapes and complex sub-structures. Fig. 12, that shows 5 landforms of this group, and the blended slope map and the 3D image of Fig. 4c, indicate that ISs can be identified as a single structure (occupying all the basal area) composed of several small subunit landforms (Tanaka et al., 2003). These small landforms can be both cratered and non-cratered structures, including mounds, impact craters and peaked structures with large variability in size and shape. Nevertheless, all these small landforms were considered as elements of a bigger landform instead of individual structures. These characteristics lead us to consider these structures as a separate type of landforms.

The basal area of these landforms varies between 152.24 and 3698.85 km^2, with an average of 986.85 km^2 (see Table 2). Therefore, they are the biggest structures of our sample set. The longest basal diameter, Wco, is on average 34.176 km, and the height, Hco, 0.402 km. The height of these topographic features is similar in Olympia Undae and Scandia Cavi, as well as the elongation of their base given by the ratio between the shortest and the longest diameters (Sco/Wco ~0.76).

4.4. General comparison

We have shown in this Section that the selected structures clearly belong to six different classes with marked differences.

In terms of location (Fig. 5a), IC and IS landforms are present both in Olympia Undae and Scandia Cavi. In contrast, the SD group is only located in Olympia Undae, and the UCs, CCs and PDs are only found in Scandia Cavi. The largest amount of CCs can be found in the western part of Scandia Cavi, and the maximum number of PDs in its eastern zone. In addition, there are several UC, CC and PD landforms that can be found at the boundary transition of both regions.

In general, the areal distribution of the structures does not exhibit any linear or curvilinear pattern (Fig. 5a). The only exception are some SDs and the five ISs located near the border between Olympia Undae and

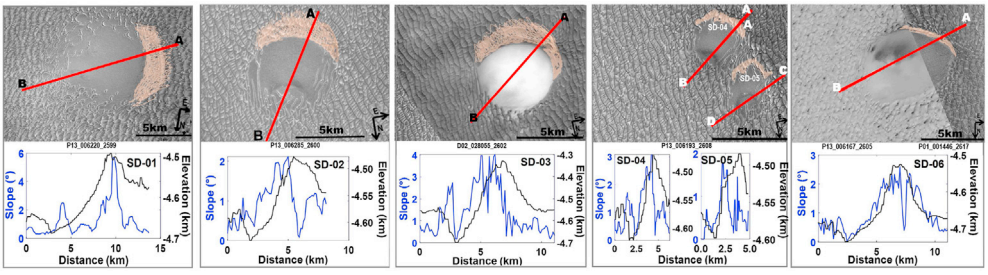

Fig. 11. Representative examples of the Simple Domes subgroup. Orbital images are shown on the top row and topographic (black) and blended slope (blue) profiles corresponding to the line marked on the images are shown in the bottom row. The pinkish area highlights the depressed zone surrounding the landform that is characteristic of this type of structures.

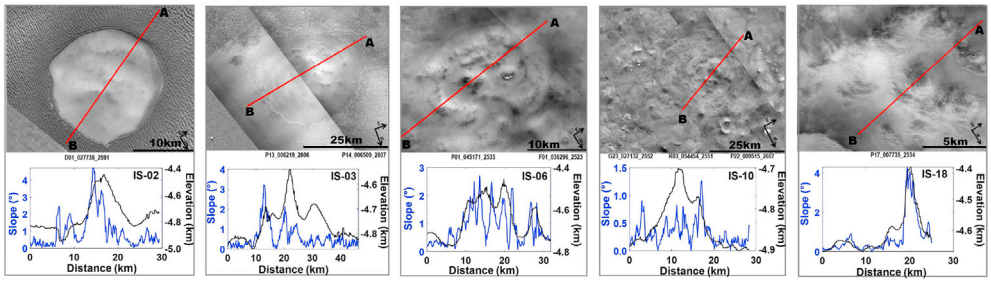

Fig. 12. Representative examples of the Irregular Structures subgroup. Orbital images are shown on the top row and topographic (black) and blended slope (blue) profiles corresponding to the line marked on the images are shown in the bottom row.

Scandia Cavi, where, as can be seen in Fig. 1, the sand layer is less thick (Tanaka et al., 2008). Some other structures could exist in the region that are not visible due to the sand layer.

Comparing the basic morphometric parameters between the six different categories, we find that cratered landforms have the largest scatter in size, while SDs and PDs are generally smaller in both horizontal and vertical dimensions. IS landforms are the biggest, and ISs and PDs have the most diverse morphology. It is important to keep in mind that the true size of some of the structures, especially those in Olympia Undae, could be somewhat greater as they might be partially buried in the sand.

Fig. 13a–c are to compare some characteristics of the non-cratered structures with those of the Irregular ones. Panel 13a displays the Wco-Sco relations in the three groups, which is linear. This indicates that in the three cases, their bases are almost circular. The distribution in the plot shows the largest size of IS landforms and the smallest of PDs. The SDs occupy an intermediate position. This distribution is also present in Fig. 13b where the topographic profiles of three representative structures are displayed. The contrast of the IS profile with those of the non-cratered structures brings to light the high complexity that IS structures can reach. In turn, Fig. 13c that represents height (Hco) versus basal area (A), shows that Peaked Domes are the highest and the Simple Domes the lowest. ISs have a 2–3 times larger diameter than PDs and SDs, and smaller heights than the highest PDs but larger than SDs. This figure also indicates that, although the mean values of PDs are similar to SDs and ISs, the main difference with them is their smaller basal area.

5. Discussion

We have performed a detailed geomorphological analysis of 200 topographic features identified in Olympia Undae and Scandia Cavi areas. This analysis has led to classifying these landforms into three main groups: cratered structures, non-cratered structures and other complex landforms named 'irregular structures'. A discussion of their possible formation processes is done in order to constrain the role they play in the geological evolution of the study area. For that, three possible origins are considered: (1) "internal" such as volcanic process; (2) "surface processes" when the phenomena occur either above its surface and close to it, such as aeolian processes that generate erosion and deposition, or just below it as CO_2 sublimation and subglacial processes; (3) "impact", when the process is originated by an impact event such as meteorites coming from comet debris, asteroids or meteoroids.

5.1. Internal processes

These are caused by the heat release through two basic mechanisms: conduction and convection from inside the planet.

Volcanic processes (including subglacial volcanoes). The comparison of CCs with similar landforms in other regions of Mars might also give insight into their origin. Cratered Cones are small to medium-sized landforms (area ranging from 4.47 to 648.40 km^2) whose morphometric characteristics and size are similar to other landforms that have been observed at other Martian locations (Fagan et al., 2010; Skinner and Tanaka, 2006). Small volcanic cones are located not only in the largest Martian volcanic provinces, i.e., Tharsis, Elysium, or in large crater basins such as Hellas, but also at several other sites scattered around the planet (Hauber et al., 2011; Brož and Hauber., 2012; Brož et al., 2015). Focusing on the diameter distribution, it can be noted that CCs have similar Wcr to the volcanic candidate cones at Isidis and Amazonis Planitiae, which diameter varies from 30 to 1000 m (Fagents et al., 2002).

Some models describing the volcanism in the circumpolar region favor the sub-ice growth of volcanoes (Head and Pratt, 2001; Hovius et al., 2008). In this process, hot lava and cold surface ice interact, producing liquid and gas phase H_2O, what could lead to explosive eruptions. The explosion would generate the crater whose initial shape and depth would be modified by processes involving ice-water phase change, induration originated by deposition of external ice, and ice-related alteration by glacial or periglacial processes (Hargitai and Kereszturi, 2015). These processes can also include sublimation of deposited ice and related collapse (Fishbaugh and Head, 2005; Fishbaugh et al., 2007; Tanaka et al., 2009; Szynkiewicz et al., 2013). The changes could be even more disruptive if these processes affect the crater subsurface fault pattern. This situation could be a possible scenario for a significant number of our CCs. It can also be an explanation for the origin of the Irregular Structures because permafrost lasts for a long period (e.g. occasionally more than a billion years) as this area had sub-zero temperatures for most of the geological history, even considering the effect of climatic changes too (Clifford et al., 2010). The eruption of mud or slurries, water and gases that drive to the formation of mud volcanoes could be further mechanisms playing a role in the formation of part of the big structures, such as the ISs (Kite et al., 2007). This can be the case of the broad hills in Olympia Undae, classified as IS in this work and considered as tholi by Tanaka et al. (2003). Slurries expelled to the surface from below could have contributed to the formation of these landforms while more energetic processes such as collapses generated by phreatic or cryoclastic eruptions, could have produced the characteristic depressions of Scandia Cavi and some of its biggest landforms.

Several examples have been studied on Mars for lava-water interactions (Squyres et al., 1987; Chapman and Tanaka, 2002; Warner and Farmer, 2010). Rootless cones can form via explosive interactions of lava and shallow subsurface ice (Lanagan et al., 2001) and is worth considering that Wcr of CCs is similar to the rootless cone candidates with ~100 m diameter at Amazonis Planitia (Greeley and Fagents, 2001).

The presence of different subglacial volcanic structures is confirmed both on Earth (Pedersen and Grosse, 2014) and Mars (Ghatan and Head, 2002; Pedersen, 2016). Fagan et al. (2010) studied four landforms within this region, of which two correspond to CC-05 and CC-06 established in this study. Those authors classify these landforms as steep-sided cones, which suggest possible subglacial volcanic origin.

5.2. Surface processes

Aeolian processes. Strictly speaking, Aeolian processes are not

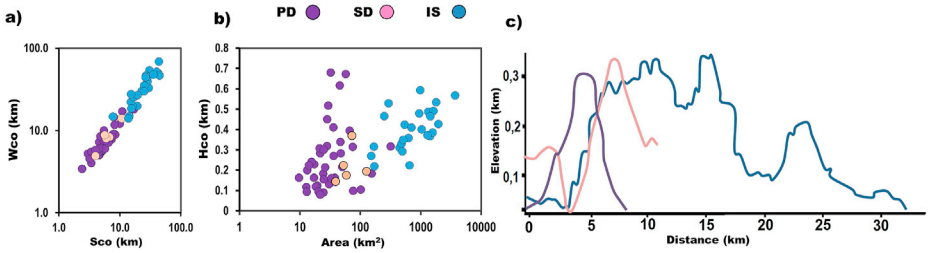

Fig. 13. Comparison of non-cratered landforms and Irregular Structures. (a)Wco versus Sco for these two groups:(b)Same for Hco versus Area, and (c) Comparison of characteristic elevation profiles with distance from three landforms belonging to these categories: PD-14, SD-03 and IS-06.

primary formation mechanisms but could have contributed to the appearance of PD and SD structures. Aeolian effects are frequent in the northern polar region of Mars (Garvin et al., 2000), and the circumpolar erg (Breed et al., 1979) with some isolated barchans (Bourke et al., 2004). These features are clearly different from the separate dunes which are characteristic of the crater interiors of the southern highlands (Fenton and Hayward, 2010). The six SDs located in Olympia Undae between 79° and 81° N are situated 50 km from each other. Their arc-shaped erosional "depressions" next to an elevated structure are situated on the north-eastern side (Fig. 11), which is compatible with wind-driven formation processes because, at least at present, the primary wind has this direction (Ewing et al., 2010; Hayward et al., 2014; Fernandez-Cascales et al., 2018). Therefore, the primary wind could have played a role in their formation, but aeolian mechanisms were probably not the only forces at work. Half of the SDs (SD-02, SD-04 and SD-05, Fig. 11) have a crescent shape with arc-shaped missing parts in the northeastern section. They partly resemble horseshoe-shaped barchan dunes (Bourke and Balme, 2008) and their size (4–15 km) is around the upper limit of the diameter range for barchans on Mars (Parteli et al., 2014). Their height varies between 146 and 369 m, greater than those assumed for Mars (Bourke et al., 2006). Surrounding trenches are present in the case of four of the landforms of this type, what might be linked to climate-related processes such as oriented deposition and sublimation of volatiles around heights, partly similar to other sublimation-related depressions at middle- and high-latitude terrains of Mars (Zanetti et al., 2010).

Erosion, exhumation and sublimation. As commented before, the analysis carried out with the Mars Reconnaissance Orbiter Shallow Radar (SHARAD) over the northern polar area by Nerozzi and Holt (2019) points to the fact that layers of water ice were deposited in the Vastitas Borealis Interior Unit and superimposed to sand sediments that experimented cementing processes. The CO_2 ice is deposited and when the temperature increases (Buhler and Piqueux, 2021), sublimates below the CO_2 layer eroding the structures, and modifying their shape. In some cases, structures with greater depths of crater and size, such as the impact craters Dokka (IC-05) and Jojutla (IC-08) accumulate water ice inside as studied by Conway et al. (2012). Our entire study area has been influenced by these processes that affect the shape of all kinds of structures and produce irregularities in the profiles of deep craters. These processes keep acting presently and, therefore, the formation of each structure should be studied individually, but this is not the subject of this paper.

5.3. Impact processes

Impact craters can also witness alteration processes similar to those described above and according to the study of Conway et al. (2012) the shape alteration of deep impact craters with ice-rich mounds inside is due to the CO_2, water ice and sublimed H_2O interactions driven by seasonal environmental changes.

The IC landforms could be related to five types of morphological characteristics originated by impacts: "round crater", "excess ejecta", "perched", "pedestal" (Kadish and Head 2011, 2014) and "ellipsoidal" (Chappelow and Herrick, 2008) craters. In the first two types, the impact excavates both an ice-rich mantle and a silicate regolith layer (Kadish and Head, 2011). The ejected rocky material covers the icy layer and preserves it from sublimation. Consequently, either it generates an excess ejecta crater (Black and Stewart, 2008) or a perched crater if a subsequent infilling process occurs, elevating the crater surface over the surrounding terrain. Excess ejecta craters are younger and deeper than perched ones and can be distinguished as the ejecta is up and under the terrain's topographic level. For example, IC-12, IC-15, IC-17 and IC-30 are representative examples of this type of ICs (see Fig. S2 of the Supporting Information File).

Perched craters are older landforms with a characteristic profile of an ejecta zone and a shallow crater located over the surface level (Boyce et al., 2005; Garvin et al., 2000b; Meresse et al., 2006; Kadish and Head 2011, 2014). IC-04, IC-10, IC-11, IC-14 and IC-20 are examples of this subgroup. As commented in Section 4.1.2., impact-related landforms are also distinguishable from the CCs because they have a deeper crater. In this study, the crater depth difference when comparing IC and CC landforms with a similar Wcr can reach 100 m. In some cases, small perched craters can be confused with CC or some UC, because the sediments and dunes can hide the ejecta material.

Pedestal craters are shallower craters able to decrease the sublimation rate of the surrounding terrain (Kadish and Head, 2011) covered and shielded by their ejecta. The result is a characteristic pedestal shape with a sharp topographic step at its edge that allows distinguishing these topographic landforms from CCs, in spite of their shallow craters. For example, landforms IC-09 and IC-27 are clear pedestal craters.

In some cases, the discrimination between CCs and ICs can be made by paying attention to the shapes of the rim and the ejecta. For instance, craters with an ellipsoidal rim and "butterfly" ejecta can indicate that they originate from a low-angle impact (Chappelow and Herrick, 2008). This could be the case of the double crater located on a flat plain at (40.5°N, 222.5°E), attributed to an impacting body as asteroid or comet fragments. This landform has been classified in this study as an undifferentiated structure (UC-03, Fig. 8) because it lacks a clear ejecta.

Some of the landforms of this study have been previously analyzed by other authors. In particular, Garvin et al. (2000b) studied the landforms called IC-4, IC-5, IC-8, IC-11 and IC-29 in our study, and also agreed with our interpretation considering them as ICs. In a similar way, Fagan and Sakimoto (2012) examined 346 circumpolar ICs located in the latitude range of 57–82°N, of which 9 agree with structures of our IC group in their classification.

5.4. Combination of processes

Based on the cases discussed above, none of the proposed formation processes alone account for the origin of the studied landforms. Although volcanic processes appear to be a relevant mechanism, especially for CCs landforms, other processes could be also involved in the formation of these landforms. For example, CC-05 in Fig. 6a shows some fine-scaled parallel stripes that look like layering, likely composed of a dust and ice mixture, formed by depositional processes partly similar to the latitude-dependent mantle (LDM) (Kreslavsky and Head, 2002; Orgel et al., 2019).

A combination of processes can also explain the origin of the non-

cratered landforms and the Irregular Structures. As SDs are surrounded by dunes and situated closer to the polar cap, sedimentary or erosional processes driven by katabatic and seasonal winds, what could be important to shape their morphology (Herny et al., 2016; Spiga and Smith, 2018). As commented above, climate-related processes such as oriented deposition and sublimation of volatiles around heights could contribute to the formation too. In turn, the large complexity of IS landforms suggests an origin involving various processes such as hydrothermal phenomena (Tanaka et al., 2008), mud dome generation (Kite et al., 2007; Skinner and Mazzini, 2009; Hargitai and Kereszturi, 2015) and volcano-ice interaction. Nerozzi and Holt (2019) showed that subsurface ice exists in the region, which supports volcano-ice interaction.

PDs seem to have a primary internal origin, probably connected to volcanic episodes but they could also be affected by erosional mechanisms. Their steep slopes indicate that the consistency of their material is higher than the other categories and that their formation processes could be substantially different from the other domes less steep. Landforms without craters like PD-28 could be compatible with characteristics of pingos that are elevated ice cored hills with roughly circular shape. Occasionally, they show fractures or a central depression at their top, somewhat similar to a volcanic cone. They form at periglacial terrains, where ice or water is present in the subsurface (Burr et al., 2009). This liquid or solid-plastic ice accumulates as a lens-shaped structure below, or the water freezes and expands. In both cases the final result is a rise of the surface of the landform producing a dome shape.

5.5. Circumpolar gypsum

The general consequence of subsurface interaction is expected to be hydrothermal circulation of liquid water, which happened on Mars even during the Amazonian period (McCubbin et al., 2010). Sulfates found at high latitude in the Southern Hemisphere, particularly in the Sisyphi Montes (70°S, 13°E), were attributed to subglacial volcanism (Ackiss et al., 2018; Ackiss, 2019) although other volcanic processes such as subaerial hydrothermal alteration cannot be discarded (Ackiss and Wray, 2014). While the origin of gypsum in the northern circumpolar area is not necessarily related to hydrothermal alteration, the expected presence of permafrost with possible joint occurrence of volcanic/magmatic activity support subsurface hydrothermal processes. Such interaction could also be related to the formation of gypsum deposits in Olympia Undae (Langevin et al., 2005). Gypsum concentration decreases in this region from its eastern edge toward the west, following the inferred wind direction (Langevin et al., 2005; Fishbaugh et al., 2007), which proves that its distribution is closely related to aeolian activity (Feldman et al., 2008). The suggested gypsum formation processes involve either local or allochthonous origin and could be produced by local evaporitic deposition in interdune areas (Fishbaugh et al., 2007; Szynkiewicz et al., 2010), or erosion from a local gypsum-rich underlying unit (Tanaka, 2006).

A possible volcanic field could be connected to the heat allowing the water ice to melt, the volcanic materials to be altered and the sulfur input to create acid weathering conditions. This would lead, among other factors, to the formation of gypsum (Tréguier et al., 2008; Berger et al., 2009). Overall, the conditions required to produce gypsum in this kind of scenario are very similar to the current conditions encountered at the surface of Mars for most of the Late Amazonian period (Góbi and Kereszturi, 2019). The only notable exception is the SO_2 that may be provided by episodic volcanic activity, which is consistent with the young age of both the gypsum-rich dunes and the CC landforms described in this paper. Alternatively, hydrothermal activity associated with the CC landforms could also provide the sulfur input needed to produce gypsum (Ackiss, 2019). The allochtonous hypothesis assumes that the alteration of volcanic material that came from Alba Patera (Tanaka, 2006) could lead to the formation of gypsum and trapped gypsum crystals could be consequently released from the sublimation-induced alteration of the polar cap (Massé et al., 2012). This hypothesis has received support from studies suggesting that gypsum appears to be resistant to erosion during long-distance wind transport (Szynkiewicz et al., 2013).

5.6. Future studies

Further study is required to determine which of the above listed hypotheses is the most likely to occur. The possible presence of gullies in several of the cratered landforms could also be further investigated as these are important in astrobiological research (e.g. Cabrol et al., 2001; Pablo and Fairén, 2004; Núñez et al., 2016; Pal, 2019). Subsurface radar investigations such as those carried out with the Mars Advanced Radar for Subsurface and Ionosphere Sounding (MARSIS) could clarify their origin through a detailed survey of the subsurface of these landforms. High-resolution images in this area recorded under proper illumination conditions, without wintertime frost coverage, may provide evidence of gypsum occurrence as outcrops at ice/rock interfaces. Well targeted High Resolution Imaging Science Experiment (HiRISE) images also offer valuable information that can be useful to get this aim. Upcoming orbital missions may play a decisive role in achieving this objective.

6. Conclusions

A systematic analysis of the morphology of 200 small-to-medium size landforms in Olympia Undae and Scandia Cavi regions has been performed using images from Mars Express and MRO, along with topographic information from MGS. This analysis drives the classification of these newly identified landforms into three groups: (1) cratered structures, (2) non-cratered structures, and (3) irregular structures. The first group is composed by three subgroups (Cratered Cones, Impact Craters and Undifferentiated craters) and the second by two (Peaked Domes and, Simple Domes), while the last one remains without any subdivision. The possible relation of these 200 structures to internal, surface, and impact processes is discussed and it could be established that combined interactions among these three types of processes seem to offer the best explanation for many of the identified landforms.

Declaration of competing interest

The authors declare that they have no known competing financial interests or personal relationships that could have appeared to influence the work reported in this paper.

Acknowledgements

MH is grateful for the help received from the Spanish project RTI 2018-094827-B-C21; BS-C acknowledges support through UK-STFC Ernest Rutherford Fellowship ST/V004115/1 and STFC grant ST/S000429/1. AK acknowledges the support of GINOP-2.3.2-15-2016-00003 project by NKFIH. Authors express their gratitude to J. Martínez-Frías and Allison Graettinger for their very useful advice. JMARS is gratefully acknowledged. All data from Mars Express were downloaded from the ESA Planetary Science Archive (https://www.cosmos.esa.int/web/psa/mars-express). The rest of the data were downloaded from the JMARS online site (https://jmars.asu.edu/). The dataset produced by this study, as well as the JMARS map with all the landforms, are freely available at Sánchez-Bayton et al. (2021).

Appendix A. Supplementary data

Supplementary data to this article can be found online at https://doi.

org/10.1016/j.pss.2021.105389.

References

Ackiss, S.E., Wray, J.J., 2014. Occurrences of possible hydrated sulfates in the southern high latitudes of Mars. Icarus 243, 311–324. https://doi.org/10.1016/j.icarus.2014.08.016.

Ackiss, S.E., Horgan, B., Seelos, F., Farrand, W., Wray, J., 2018. Mineralogic evidence for subglacial volcanism in the Sisyphi Montes region of Mars. Icarus 311, 357–370.

Ackiss, S.E., 2019. Investigating the Mineralogy and the Morphology of Subglacial Volcanoes on Earth and Mars, PhD Thesis. Purdue University.

Aharonson, O., Zuber, M.T., Rothman, D.H., 2001. Statistics of mars' topography from the mars orbiter laser altimeter: slopes, correlations, and physical models. J. Geophys. Res. 106, 23723–23735. E10.

Berger, G., Toplis, M.J., Tréguier, E., D'Uston, Claude, Pinet, P., 2009. Evidence in favor of small amounts of ephemeral and transient water during alteration at Meridiani Planum, Mars. Am. Mineral. 94 (8–9), 1279–1282. https://doi.org/10.2138/am.2009.3230.

Black, B.A., Stewart, S.T., 2008. Excess ejecta craters record episodic ice-rich layers at middle latitudes on Mars. J. Geophys. Res. 113 (E2). https://doi.org/10.1029/2007JE002888. Cite ID E02015.

Boazman, S.J., Grindrod, P.M., Balme, M.R., Vermeesch, P., Davis, J.M., Baird, T.R., Silvestro, S., Cho-jnacki, M., Vaz, D.A., Cardinale, M., Esposito, F., 2020. Polar dune migration at scandia cavi, mars: the effects of seasonal processes. 51st Lunar and Planetary Science Conference.

Bourke, M.C., Balme, M., Zimbelman, J., 2004. A Comparative Analysis of Barchan Dunes in the Intra-crater Dune Fields and the North Polar Sand Sea. 35th Lunar and Planetary Science Conference abstract 1453.

Bourke, M.C., Balme, M., Beyer, R., Williams, K., Zimbelman, J., 2006. A comparison of methods used to estimate the height of sand dunes on Mars. Geomorphology 81, 440–445. https://doi.org/10.1016/j.geomorph.2006.04.023.

Bourke, M.C., Balme, M., 2008. Megabarchans on Mars. Lunar and Planetary Science Conference abstract 7036.

Boyce, J.M., Mouginis-Mark, P., Garbeil, H., 2005. Ancient oceans in the northern lowlands of Mars: evidence from impact crater depth/diameter relationships. J. Geophys. Res. 110. https://doi.org/10.1029/2004JE002328.

Breed, C., Grolier, M.J., Mccauley, J.F., 1979. Morphology and distribution of common 'sand' dunes on mars: comparison with the Earth. J. Geophys. Res. 84 B14, 8183–8203.

Brož, P., Hauber, E., 2012. A unique volcanic field in Tharsis, Mars: pyroclastic cones as evidence for explosive eruptions. Icarus 218 (1), 88–99. https://doi.org/10.1016/j.icarus.2011.11.030. March 2012.

Brož, P., Hauber, E., 2013. Hydrovolcanic tuff rings and conesas indicators for phreatomagmaticexplosive eruptions on Mars. J. Geophys. Res.: Plan 118, 1656–1675. https://doi.org/10.1002/jgre.20120,2013.

Brož, P., Čadek, O., Hauber, E., Pio Rossi, A., 2015. Scoria cones on Mars: detailed investigation of morphometry based on high-resolution digital elevation models. J. Geophys. Res. 120, 1512–1527. https://doi.org/10.1002/2015JE004873.

Buhler, P.B., Piqueux, S., 2021. Obliquity-driven CO_2exchance between Mars atmosphere; regolith, and polar cap. Journal of Geophisical Research: Planet 126. https://doi.org/10.1029/2020JE006759.

Burr, D.M., L, K., Tanaka, K. Yoshikaw, 2009. Pingos on Earth and Mars Planetary and Space Science 57, 541–555. https://doi.org/10.1016/j.pss.2008.11.003.

Cabrol, N.A., Wynn-Williams, D., Crawford, D.A., Grin, E., 2001. Recent aqueous environments in martian impact craters: an astrobiological perspective. Icarus 154 (1), 98–112. https://doi.org/10.1006/icar.2001.6661.

Chapman, M.G., Tanaka, K.L., 2002. Related magma-ice interactions: possible origins of chasmata, chaos, and surface materials in Xanthe, margaritifer, and meridiani terrae, mars. Icarus 155, 324–339. https://doi.org/10.1006/icar.2001.6735.

Chappelow, J.E., Herrick, R.R., 2008. On the origin of a double, oblique impact on Mars. Icarus 197, 452–457. https://doi.org/10.1016/j.icarus.2008.06.00.

Chicarro, A., Martin, P., Traunter, R., 2004. Mars Express: A European Mission to the Red Planet SP-1240. Eur. Space Agency Publ. Div., Noordwijk, Netherlands, pp. 3–16.

Christensen, P., Engle, E., Anwar, S., Dickenshied, S., Noss, D., Gorelick, N., Weiss-Malik, M., 2009. JMARS - A Planetary GIS. American Geophysical Union, Fall Meeting 2009 abstract #IN22A.

Clifford, S.M., Lasue, J., Heggy, E., Boisson, J., McGovern, P., Max, M.D., 2010. Depth of the Martian cryosphere: revised estimates and implications for the existence and detection of subpermafrost groundwater. J. Geophys. Res. 115 (E7), E003462.

Conway, S.J., Hovius, N., Barnie, T., Besserer, J., LeMouélic, S., Orosei, R., Read, N.A., 2012. Climate-driven deposition of water ice and the formation of mounds in craters in Mars' North Polar region. Icarus 220, 174–193. https://doi.org/10.1016/j.icarus.2012.04.021.

Ewing, R.C., Peiret, A.B., Kocurek, G., Bourke, M., 2010. Dune field pattern formation and recent transporting winds in the Olympia Undae Dune Field, north polar region of Mars. J. Geophys. Res. 115, E08005. https://doi.org/10.1029/2009JE003526, 2010.

Fagan, A.L., Sakimoto, S.E.H., Hughes, S.S., 2010. Formation constraints on Martian north polar volcanic landforms. J. Geophys. Res. 115. https://doi.org/10.1029/2009JE003476.

Fagan, A.L., Sakimoto, S.E.H., 2012. An investigation of Martian northern high-latitude and polar impact crater interiors: atypical interior topographic features and cavity wall slopes. Meteoritics Planet Sci. 47 (6), 970–991. https://doi.org/10.1111/j.1945-5100.2012.01365.x.

Fagents, S.A., Pace, K., Greeley, R., 2002. Origins of Small Volcanic Cones on Mars. 33th Lunar and Planetary Science Conference abstract 1594.

Feldman, W.C., Bourke, M.C., Elphic, R.C., Maurice, S., Bandfield, J., Prettyman, T.H., Diez, B., Lawrence, D.J., 2008. Hydrogen content of sand dunes within Olympia Undae. Icarus 196, 422–432. https://doi.org/10.1016/j.icarus.2007.08.044.

Fenton, L.K., Hayward, R.K., 2010. Southern high latitude dune fields on Mars: morphology, aeolian inactivity, and climate change. Geomorphology 121, 98–121. https://doi.org/10.1016/j.geomorph.2009.11.006.

Fernandez-Cascales, L., Lucas, A., Rodriguez, S., Gao, X., Spiga, A., Narteau, C., 2018. First quantification of relationship between dune orientation and sediment availability, Olympia Undae, Mars. Earth Planet Sci. Lett. 489, 241–250. https://doi.org/10.1016/j.epsl.2018.03.001.

Fishbaugh, K.E., Head, J.W., 2005. Origin and characteristics of the Mars north polar basal unit and implications for polar geologic history. Icarus 174, 444–474. https://doi.org/10.1016/j.icarus.2004.06.021.

Fishbaugh, K.E., Poulet, F., Langevin, Y., Chevrier, V., Bibring, J.-P., 2007. The origin of gypsum in the Mars north polar region. J. Geophys. Res. 112, E07002. https://doi.org/10.1029/2006JE002862.

Garvin, J.B., Sakimoto, S.E.H., Frawley, J.J., Schnetzler, C.C., Wright, H.M., 2000a. Topographic evidence for geologically recent near-polar volcanism on mars. Icarus 145, 648–652. https://doi.org/10.1006/icar.2000.6409.

Garvin, J.B., Sakimoto, S.E.H., Frawley, J.J., Schnetzler, C., 2000b. north polar region craterforms on mars: geometric characteristics from the mars orbiter laser altimeter. Icarus 144, 329–352. https://doi.org/10.1006/icar.1999.6298.

Ghatan, G.J., Head III, J.W., 2002. Candidate subglacial volcanoes in the south polar region of Mars: morphology, morphometry, and eruption conditions. J. Geophys. Res. 107 (E7), 5048. https://doi.org/10.1029/2001JE001519.

Góbi, S., Kereszturi, A., 2019. Analyzing the role of interfacial water on sulfate formation on present Mars. Icarus 322, 135–143. https://doi.org/10.1016/j.icarus.2019.01.005.

Greeley, R., Fagents, S.A., 2001. Icelandic pseudocraters as analogs to some volcanic cones on Mars. J. Geophys. Res. 106 (E9), 20509–20628. https://doi.org/10.1029/2000JE001378.

Hargitai, H., Kereszturi, A. (Eds.), 2015. Encyclopedia of Planetary Landforms. Springer, New York Heidelberg Dordrecht London.

Hauber, E., Brož, P., Jagert, F., Jodłowski, P., Platz, T., 2011. Very recent and wide-spread basaltic volcanism on Mars. Geophys. Res. Lett. 38. https://doi.org/10.1029/2011GL047310.

Hayward, R.K., Fenton, L.K., Titus, T.N., 2014. Mars global digital dune database (MGD^3): global dune distribution and wind pattern observations. Icarus 230, 38–46. https://doi.org/10.1016/j.icarus.2013.04.011.

Head, J.W., Pratt, S., 2001. Extensive Hesperian-aged south polar ice sheet on Mars: evidence for massive melting and retreat, and lateral flow and ponding of meltwater. J. Geophys. Res. 106 (E6), 12275–12300. https://doi.org/10.1029/2000JE001359.

Herny, C., Carpy, S., Bourgeois, O., Spiga, A., Rodriguez, S., Massé, M., Le Mouélic, S., 2016. The role of sublimation and condensation in the dynamics of aeolian ice sedimentation waves on the north polar cap of Mars. Sixth International Conference on Mars Polar Science and Exploration. Ab. #6075. https://www.hou.usra.edu/meetings/marspolar2016/pdf/6075.pdf.

Horgan, B.H., Bell III., J.F., Noe Dobrea, E.Z., Cloutis, E.A., Bailey, D.T., Craig, M.A., Roach, L.H., Mustard, J.F., 2009. Distribution of hydrated minerals in the north polar region of Mars. J. Geophys. Res. 114. https://doi.org/10.1029/2008JE003187.

Hovius, N., Lea-Cox, A., Turowski, J.M., 2008. Recent volcano ice interaction and outburst flooding in a Mars polar cap re-entrant. Icarus 197 (1), 24–38. https://doi.org/10.1016/j.icarus.2008.04.020.

Kadish, S.J., Head, J.W., 2011. Impacts into non-polar ice-rich paleodeposits on Mars: excess ejecta craters, perched craters and pedestal craters as clues to Amazonian climate history. Icarus 215 (1), 34–46. https://doi.org/10.1016/j.icarus.2011.07.014.

Kadish, S.J., Head, J.W., 2014. The ages of pedestal craters on Mars: evidence for a late-Amazonian extended period of episodic emplacement of decameters-thick mid-latitude ice deposits. Planet. Space Sci. 91, 91–100. https://doi.org/10.1016/j.pss.2013.12.003.

Kite, E.S., Hovius, N., Hiller, J.K., Besserer, J., 2007. Candidate mud volcanoes in the northern plains of Mars. Eos Trans. AGU 88, 52. Fall Meet. Suppl., Abstract V13B-1346.

Kneissl, T., Neukum, G., 2008. New investigations of possible volcanic landforms at the886Martian north Pole - first results. LPSC 39, 1319.

Krasilnikov, S., Kuzmin, R., Evdokimova, N., 2018. Remnant massifs of layered deposits at high northern latitudes of mars. Sol. Syst. Res. 52 (1), 26–36. ISSN 0038-0946.

Kreslavsky, M.A., Head, J.W., 2002. Mars: nature and evolution of young latitude-dependent water-ice-rich mantle. Geophys. Res. Lett. 29 (15). https://doi.org/10.1029/2002GL015392.

Lanagan, Peter D., McEwen, Alfred S., Keszthelyi, Laszlo P., Thordarson, Thorvaldur, 2001. Rootless cones on Mars indicating the presence of shallow equatorial ground ice in recent times. Geophys. Res. Lett. 28, 2365–2367. https://doi.org/10.1029/2001GL012932.

Langevin, Y., Poulet, F., Bibring, J., Gondet, B., 2005. Sulfates in the north polar region of mars. Detected by OMEGA/mars express. Science 307, 5715.

Lenhardt, N., Borahb, S., Lenhard, Z., Bumby, A., Ibinoof, M., Salih, S., 2018. The monogenetic Bayuda Volcanic Field, Sudan–New insights intogeology and volcanic morphology. J. Volcanol. Geoth. Res. 356, 211–224. https://doi.org/10.1016/j.jvolgeores.2018.03.010.

Malin, M., Bell, J., Cantor, B., Caplinger, M., Calvin, W., Clancy, T., Edgett, K., Edwards, L., Haberle, R., James, P., Lee, S., Ravine, M., Thomas, P., Wolff, M., 2007. Context camera investigation on board the mars reconnaissance orbiter. J. Geophys. Res. 112, E05S04. https://doi.org/10.1029/2006JE002808.

Massé, M., Bourgeoisa, O., Le Mouélica, S., Verpoorterc, C., Pigad, A.S.-, Le Deite, L., 2012. Wide distribution and glacial origin of polar gypsum on Mars. Earth Planet Sci. Lett. 317 (31), 44–55. https://doi.org/10.1016/j.epsl.2011.11.035.

McEwen, A.S., Banks, M.E., Baugh, N., Becker, K., Boyd, A., et al., 2010. The high resolution imaging science experiment (HiRISE) during MRO's primary science phase (PSP). Icarus 205 (1). https://doi.org/10.1016/j.icarus.2009.04.023, 2-37, ISSN 0019-1035.

McCubbin, F.M., Smirnov, A., Nekvasil, H., Wang, J., Hauri, E., Lindsley, D.H., 2010. Hydrous magmatism on Mars: a source of water for the surface and subsurface during the Amazonian. Earth Planet Sci. Lett. 292 (1–2), 132–138. https://doi.org/10.1016/j.epsl.2010.01.028.

Meresse, S., Costard, F., Mangold, N., Baratoux, D., Boyce, J.M., 2006. Martian perched craters and large ejecta volume: evidence for episodes of deflation in the northern lowlands. Meteoritics Planet Sci. 41, 1647–1658. https://doi.org/10.1111/j.1945-5100.2006.tb00442.x.

Nerozzi, S., Holt, J.W., 2019. Buried ice and sand caps at the north pole of Mars: revealing a record of climate change in the cavi unit with SHARAD. Geophys. Res. Lett. https://doi.org/10.1029/2019GL082114 accepted.

Neukum, G., Jaumann, R., HRSC Co-Investigator and Experiment Team, 2004a. HRSC: the high resolution stereo camera of mars express. In: Wilson, A. (Ed.), Mars Express: the Scientific Payload, pp. 17–35. Noordwijk, The Netherlands: ESA. https://www.esa.int/esapub/sp/sp1240/sp1240web.pdf.

Neukum, J.G., Jaumann, R., Hoffmann, H., Hauber, E., Head, J.W., Basilevsky, A.T., Ivanov, B.A., Werner, S.C., Van Gasselt, S., Murray, J.B., McCord, T., 2004b. Recent and episodic volcanic and glacial activity on mars revealed by the high resolution stereo camera. Nature 432, 971–979. https://doi.org/10.1038/nature03231.

Núñez, J.I., Barnouin, O.S., Murchie, S.L., Seelos, F.P., McGovern, J.A., Seelos, K.D., Buczkowski, D.L., 2016. New insights into gully formation on Mars: constraints from composition as seen by MRO/CRISM. Geophys. Res. Lett. 43, 8893–8902. https://doi.org/10.1002/2016GL068956.

Orgel, C., Hauber, E., van Gasselt, S., Reiss, D., Johnsson, A., Ramsdale, J.D., Smith, I., Swirad, Z.M., Séjourné, A., Wilson, J.T., Balme, M.R., Conway, S.J., Costard, F., Eke, V.R., Gallagher, Kereszturi, Á., Losiak, A., Massey, R.J., Platz, T., Skinner, J.A., Teodoro, L.F.A., 2019. Gridmapping the northern plains of mars: a new overview of recent water- and ice-related landforms in acidalia Planitia. J. Geophys. Res.: Plan 124 (2), 454–482. https://doi.org/10.1029/2018JE005664.

Pal, B., 2019. Global Distribution of Near-Surface Relative Humidity Levels on Mars. 50th Lunar and Planetary Science Conference abstract 1831.

Pablo, M., Fairén, A., 2004. Atlantis basin, sirenum terrae, mars: geological setting and astrobiological implications. Int. J. Astrobiol. 3 (3), 257–263. https://doi.org/10.1017/S147355040400196X.

Parteli, Eric J.R., Durán, Orencio, Bourke, Mary C., Tsoar, Haim, Pöschel, Thorsten, Herrmann, Hans, 2014. Origins of barchan dune asymmetry: insights from numerical simulations. Aeolian Research 12, 121–133. https://doi.org/10.1016/j.aeolia.2013.12.002.

Pedersen, G.B.M., Grosse, P., 2014. Morphometry of subaerial shield volcanoes and glaciovolcanoes from Reykjanes Peninsula, Iceland: effects of eruption environment. JVGR 282, 115–133. https://doi.org/10.1016/j.jvolgeores.2014.06.008.

Pedersen, G.B.M., 2016. Semi-automatic classification of glaciovolcanic landforms: an object-based mapping approach based on geomorphometry. JVGR 311, 29–40. https://doi.org/10.1016/j.jvolgeores.2015.12.015.

Putzig, N., Smith, I., Perry, M., Foss, F., Campbell, B., Phillips, R., Seu, R., 2018. Three-dimensional radar imaging of structures and craters in the Martian polar caps. Icarus 308, 138–147. https://doi.org/10.1016/j.icarus.2017.09.023.

Rodriguez, J., Tanaka, K., Bramson, A., Leonard, G., Baker, V., Zarroca, M., 2021. North polar trough formation due to in-situ erosion as a source of young ice in mind-latitudinal mantles and Mars. Sci. Rep. 11. https://doi.org/10.1038/s41598-83329-3. Article number 6750.

Skinner, J.A., Tanaka, K.L., 2006. Evidence for and implications of sedimentary diapirism and mud volcanism in the southern Utopia highland lowland boundary plain, Mars. Icarus 186, 41–59. https://doi.org/10.1016/j.icarus.2006.08.013.

Sánchez-Bayton, Marina, Herraiz, Miguel, Martin, Patrick, Sanchez-Cano, Beatriz, Tréguier, Erwan, Kereszturi, Akos, 2021. Small and Medium Size Landforms in Scandia Cavi and Olympia Undae, Northern Circumpolar Region of Mars. University of Leicester. Dataset.

Skinner, J.A., Hare, T.M., Tanaka, K.L., 2006. Digital renovation of the atlas of Mars 1: 15,000,000-scale global geologic series maps. Lunar Planet. Sc. XXXVII abstract 2331.

Skinner, J.A., Mazzini, A., 2009. Martian mud volcanism—terrestrial analogs and implications for formational scenarios. Mar. Petrol. Geol. 26, 1866–1878. https://doi.org/10.1016/j.marpetgeo.2009.02.006.

Smith, D.E., Zuber, M.T., 1999. The Relationship of the MOLA Topography of Mars to the Mean Atmospheric Pressure. American Astronomical Society. DPS meeting #31, #67.02.

Smith, D.E., Sjogren, W.L., Tyler, G.L., Balmino, G., Lemoine, F.G., Konopliv, A.S., 1999. The gravity field of mars: results from mars global surveyor. Science 286 (5437), 94–97. https://doi.org/10.1126/science.286.5437.94.

Smith, D.E., Zuber, M., Frey, H., Garvin, J., Head, J., Muhleman, D., Pettengill, G., Phillips, R., Solomon, S., Zwally, H., Banerdt, W., Duxbury, T., Golombek, M., Lemoine, F., Neumann, G., Rowlands, D., Aharonson, O., Ford, P., Ivanov, A., Johnson, C., McGovern, P., Abshire, J., Afzal, R., Sun, X., 2001. Mars orbiter laser altimeter: experiment summary after the first year of global mapping of mars. J. Geophys. Res. 106 (E10), 23689–23722. https://doi.org/10.1029/2000JE001364.

Spiga, A., Smith, I., 2018. Katabatic jumps in the Martian northern polar regions. Icarus 308, 197–208. https://doi.org/10.1016/j.icarus.2017.10.021.

Squyres, S.W., Wilhelms, D.E., Moosman, A.C., 1987. Large-scale volcano-ground ice interactions on Mars. Icarus 70, 385–408. https://doi.org/10.1016/0019-1035(87)90085-6.

Szynkiewicz, A., Modelska, M., Buczynski, S., Borrok, D., Pratt, L., 2010. Sulfide Weathering in the Werenskioldbreen, Spitsbergen - A Polar Terrestrial Analogue for Gypsum Deposition in the North Polar Region of Mars. American Geophysical Union, Fall Meeting 2010 abstract P13B-1382.

Szynkiewicz, A., Modelska, M., Buczyński, S., Borrok, D.M., Merrison, J.P., 2013. The polar sulfur cycle in the Werenskioldbreen, Spitsbergen: possible implications for understanding the deposition of sulfate minerals in the North Polar Region of Mars. Geochem. Cosmochim. Acta 106, 326–343. https://doi.org/10.1016/j.gca.2012.12.041.

Tanaka, K.L., Skinner, J.A., Hare, T.M., Joyal, T., Wenker, A., 2003. Resurfacing history of the northern plains of Mars based on geologic mapping of Mars Global Surveyor data. J. Geophys. Res. 108. https://doi.org/10.1029/2002JE001908.

Tanaka, K.L., 2006. Mars' north polar gypsum: possible origin related to early amazonian magmatism at Alba Patera and aeolian mining. Fourth Int. Conf. Mars Polar Sci. Explor. 1323, 8024. Davos, Switzerland; LPI Contribution N°.

Tanaka, K.L., Skinner, A., Trent, M., 2005. Geologic Map of the Northern Plains of Mars Pamphlet to Accompany Scientific Investigations Map 2888.

Tanaka, K.L., Rodriguez, J.A.P., Skinner, J.A., Bourkeb, M.C., Fortezzo, C.M., Herkenhoff, K.E., Kolb, E.J., Okubo, C.H., 2008. North polar region of Mars: advances in stratigraphy, structure, and erosional modification. Icarus 196, 318–358. https://doi.org/10.1016/j.icarus.2008.01.021.

Tanaka, K.L., Rodriguez, J.A.P., Fortezzo, C.M., Seelos, F., 2009. Obliquity-driven periods of extended erosion and deposition in the geologic record of Planum boreum, mars. 40th lunar and planetary science conference. LPI 40, 2476T.

Tréguier, E., D'Uston, C., Pinet, P., Berger, G., Toplis, M.J., McCoy, T.J., Gellert, R., Brückner, J., 2008. Overview of Mars surface geochemical diversity through Alpha Particle X-Ray Spectrometer data multidimensional analysis: first attempt at modeling rock alteration. J. Geophys. Res. 113. https://doi.org/10.1029/2007JE003010.

Warner, N.H., Farmer, J.D., 2010 Jun. Subglacial hydrothermal alteration minerals in Jökulhlaup deposits of Southern Iceland, with implications for detecting past or present habitable environments on Mars. Astrobiology 10 (5). https://doi.org/10.1089/ast.2009.0425, 523-47. PMID: 20624060.

Zanetti, M., Hiesinger, H., Reiss, D., Hauber, E., Neukum, G., 2010. Distribution and evolution of scalloped terrain in the southern hemisphere, Mars. Icarus 206, 691–706. https://doi.org/10.1016/j.icarus.2009.09.010.